RSC Advances

PAPER

View Article Online
View Journal | View Issue

Cite this: *RSC Adv.*, 2025, **15**, 48463

Synthesis of a 3D-interconnected hierarchical porous carbon–copper oxide nanocomposite derived from cantaloupe fruit peel for high-performance symmetric supercapacitors

Abdullah Ba shbil, Y. S. Nagaraju, D. S. Suresh, H. Ganesha, Netra Talavara,
S. P. Vijaykumar, S. Sharanappa and H. Devendrappa *

The growing demand for efficient and sustainable energy storage devices has driven researchers to develop advance materials to fulfill the global needs. In this work, a three-dimensional (3D)-interconnected hierarchical porous carbon/copper oxide (PCCuO) nanocomposite derived from cantaloupe fruit peel was synthesized by a one-step activated carbonization method. The SEM images show a well-defined macroporous morphology with a uniform distribution of copper oxide nanoparticles and clear evidence of chemical interaction and structural modification. Owing to a 3D-interconnected porous structure and a specific surface area of up to 307.29 m^2 g^{-1}, the PCCuO-0.25 electrode demonstrates exceptional electrochemical performance, achieving a specific capacitance of 673 F g^{-1} at a current density of 1.5 A g^{-1} in a 6 M KOH electrolyte. A symmetric supercapacitor utilizing PCCuO-0.25 as both positive and negative electrodes, along with a PVA/KOH gel electrolyte, attains a maximum energy density of 51.4 Wh kg^{-1} at a power density of 616.8 W kg^{-1}, showing outstanding cycle stability with a capacitance retention of 79% and a coulombic efficiency of 98.7% after 10 000 charging–discharging cycles. This study offers a comprehensive investigation into the fabrication of supercapacitors using biomass-derived materials, aiming to provide an effective approach for producing environmentally friendly, cost-efficient, and high-performance supercapacitor electrode materials.

Received 7th September 2025
Accepted 28th October 2025

DOI: 10.1039/d5ra06736g

rsc.li/rsc-advances

1 Introduction

Currently, a lot of attention has been drawn to the excessive use of fossil fuels and the resulting environmental pollution. However, extensive efforts have been made to develop a highly porous carbon-based energy material for high-performance energy storage devices with clean, sustainable, and stable systems.[1] There are various advantages of carbon-based materials such as having strong mechanical strength, chemical and physical properties. Supercapacitors (SCs), which are generally carbon-neutral energy storage devices, have gained significant attention for their wide range of applications due to their high power densities, extended cycle life, and rapid charging–discharging capability.[2] However, an increasing number of researchers have committed to finding solutions to these issues, including low electrochemical stability, insufficient energy density, and limited capacitance.[3] In order to enhance their effectiveness for energy storage purposes, the material should have a porous structure, large specific surface area, uniform pore size, excellent optical properties, and high electrical conductivity.[4] There are a variety of carbon-based substances, such as carbon aerogels, mesoporous carbons, and activated carbons, which are the prominent candidates for supercapacitor applications.[5–7] Therefore, the pursuit of attaining elevated specific capacitance using innovative porous carbon materials with enhanced physical properties is essential for achieving both substantial power density and storage capacity.[8]

Biomass-derived activated porous carbon is highly suitable due to its unique structure and interconnected mesopores arranged in a regular pattern, large surface area, low mass density, excellent chemical stability, high electrical conductivity, affordability, and environmental friendliness.[9] Among various biomass sources, cantaloupe (*Cucumis melo*) peel is regarded as an ideal candidate for the preparation of activated carbon on account of the abundance and low cost of cantaloupe peel, rich organic composition, and high potential for achieving a large specific surface area and porosity, making it suitable for various energy storage applications.[10] Utilizing cantaloupe peels not only contributes to sustainable waste management by repurposing agricultural by-products but also supports the development of eco-friendly energy storage solutions. Moreover, due to a high proportion of carbon content in cantaloupe peel and suitable structural properties, biomass cantaloupe peel-

---

Department of Physics, Mangalore University, Mangalagangothri, Mangalore-574199, India. E-mail: dehu2010@gmail.com

derived activated carbon can be regarded as a prospective material for the next generation of supercapacitors.[11] The porous structure and large surface area may have allowed more active sites that are accessible for charge accumulation. Furthermore, a hierarchical range of pore sizes (including micro, meso, and macro pores) favors the diffusion of ions between the electrolyte and the electrode during the charge–discharge processes.[12] The construction of 3D carbon superstructures is a viable strategy for increasing surface accessibility and ion transport efficiency in carbon-based materials.[13] The activation process often produces an increased number of micropores; however, it may also result in non-interconnected or inactive pores. Template methods provide superior control over the pore size of carbon materials and are classified into hard and soft template methods.[14] Furthermore, the introduction of heteroatoms through doping has proven to be a successful approach for augmenting the electrochemical reactivity of carbon-based materials.[15–17] Activation of carbonaceous materials is typically accomplished through a physical or chemical activation process. Physical activation *via* CO_2 or steam and chemical activation utilizing KOH, $ZnCl_2$, or H_3PO_4 have been extensively developed as techniques for regulating the porous architecture.[18] Among various chemical activators, potassium hydroxide (KOH) has attracted greater attention because of its high yield, more refined porous structure, and low activation temperature.[19] In order to establish strong carbon structures during the physical activation process, a significant quantity of the internal carbon mass must be removed. On the other hand, the chemical activation approach uses chemical agents as dehydrating agents to initiate pyrolytic decomposition, resulting in the formation of tar and, consequently, an increased carbon yield.[20] Carbon materials doped with metal oxide represent an effective strategy to enhance electrochemical performance. The carbon skeleton provides the main strong chemical structure with more free radicals, which can form a chemical network with metal oxides.[21] This design aimed to maximize synergistic effects in order to improve the electrochemical properties of SCs.[22] The literature reports that many transition metal oxides exhibit high specific capacitance values, rendering them valuable candidates for SC applications, including NiO, Co_3O_4, CuO, MnO_2, and ZnO.[23–27] Among them, copper oxide (CuO) stands out as a very attractive choice for nanocomposites due to its simple synthesis, abundant presence in the Earth's crust, and strong and reliable electrochemical capabilities.[28] CuO has a significant theoretical specific capacitance, but its electrical conductivity is considerably low, and its structure undergoes degradation during the electrochemical redox process.[29] In order to overcome these issues, the use of a metal oxide composite with porous carbon can enhance diffusion of ions between the electrode and the electrolyte, thereby improving the current rate and minimizing current loss at the interface due to the large surface area and decreased volumetric strain during the cycling process. The development of SC electrodes based on conductive carbon–CuO composite materials has thus received a great deal of attention in recent years, with the aim of increasing the potential window and capacitance in order to achieve higher energy density. According to recent literature on Cu_xO@NPC,[30] Cu/C,[31] CuO-AC,[32] GO-CuO,[33] SCu-HPCFs,[34] Cu-MOF/rGO (MrGO),[35] and CuO/CNTs,[36] the synthesis of biomass-derived CuO-incorporated porous carbon composites usually involves a two-step process: carbonization followed by the chemical deposition of CuO. However, this method frequently results in increased costs and pollution, which hinders sustainable development by increasing energy consumption and processing time. Moreover, the insufficient electrical conductivity and low stability of liquid electrolytes impose limitations on their storage capacity and cycling stability in supercapacitors. Therefore, it is essential to create an electrolyte with characteristics that fall within the range of the solid phase; thus, the development of a solid-state gel polymer electrolyte (GPE) would offer a viable and efficient substitute electrolyte.[37] Various polymer matrix materials have been reported for the fabrication of GPEs, such as poly(vinyl alcohol) (PVA), poly(ethylene oxide) (PEO), poly(methyl methacrylate) (PMMA), poly(vinylidene fluoride) (PVDF), and poly(acrylonitrile) (PAN). Among these, PVA is a promising option for research due to its high electrical conductivity, excellent solubility, ability to form stable layers, strong mechanical and chemical stability, good contact with electrodes/electrolytes or adhesive properties, non-toxicity, low cost, compatibility with electrode materials, low volatility, wide potential window, and superior thermal stability.[38] Additionally, novel techniques are necessary to fabricate carbon-based electrodes supported with copper oxide, featuring adjustable porous structures and optimized interface properties.

This work presents a one-step carbonization–activation synthesis method for producing 3D-interconnected hierarchical porous carbon that is embedded with copper oxide (CuO) nanoparticles, utilizing cantaloupe fruit peel as the biomass precursor, KOH as the activating agent, and CTAB as a surfactant. This method creates a high-performance nanocomposite for supercapacitor applications by combining sustainable waste valorization with an easy-to-use, energy-efficient procedure. While the *in situ* production of CuO nanoparticles contributes to pseudocapacitance and interfacial conductivity, the use of CTAB as a pore-directing agent during activation encourages the formation of a well-defined 3D hierarchical porous structure, improving ion transport and electrolyte accessibility. The PCCuO-0.25 electrode exhibits a remarkable specific capacitance of 673 F g^{-1} at a current density of 1.5 A g^{-1}. The CV curve exhibits a superior specific capacitance of 457.2 F g^{-1} at a scan rate of 10 mV s^{-1}.

A symmetric supercapacitor employing PCCuO-0.25 for both electrodes and a PVA/KOH gel electrolyte achieves an energy density of 51.4 Wh kg^{-1} at a power density of 616.8 W kg^{-1}, demonstrating significant cycling stability with 79% capacitance retention and 98.7% coulombic efficiency after 10 000 cycles. The intention of the work is to highlight the importance of applying the findings of renewable biomass resources to address sustainability issues and minimize environmental issues in relation to electrode material synthesis. During this process, cantaloupe peel undergoes decomposition, while CuO facilitates pore formation *via* redox reactions. CTAB functions as a soft template, facilitating the formation of micelles that direct the carbon structure. CTAB decomposes upon heating, resulting in the formation of mesopores previously occupied by micelles. Moreover, the inherent oxygen content of cantaloupe peel improves surface functionality and electrochemical activity without the need for outside doping agents. This process generates a 3D-interconnected hierarchical porous network, characterized by increased surface area and improved ion transport.

2 Experimental techniques

2.1 Materials used

Cantaloupe peels were extracted from cantaloupe fruit; copper(II) oxide (CuO), potassium hydroxide (KOH), *N*-cetyl-*N*,*N*,*N*-trimethylammonium bromide (CTAB), polyvinylidene fluoride (PVDF), and charcoal were purchased from Sigma Aldrich, India. Solvents like *N*-methyl-2-pyrrolidone (NMP) and distilled water (DW) were utilized in the synthesis process.

2.2 Synthesis

Typically, 0.3 g of CTAB was added to 1 M KOH and stirred until a homogeneous solution was obtained. Then, 0.25 g of CuO was added to the solution mixture and stirred for 30 min to form a uniform solution. Next, 5 g of cantaloupe peel powder was added under magnetic stirring for 30 min, followed by heating the mixture at 100 °C for a duration of 12 h in a microwave oven. Subsequently, the resulting mixture was subjected to grinding using a mortar and further subjected to carbonization in a tubular furnace at 750 °C for a duration of 1.5 h under a N_2 atmosphere. The final product was washed with distilled water and dried in an electric oven at 80 °C for a duration of 10 h, as shown in Scheme 1. Simultaneously, we prepared different CuO loadings; specifically, 0, 0.15, and 0.25 g were used for various sample preparations and were labeled as PCCuO-0, PCCuO-0.15, and PCCuO-0.25, respectively.

2.3 Characterization techniques

The chemical composition and functional groups were analyzed using a Fourier transform infrared spectrometer (FT-IR, model ALPHA BURKUE), and the X-ray diffraction (XRD, ESCALAB210) technique was utilized to obtain the crystal structure of the as-prepared material. Raman spectra were acquired using a Raman Microscope (Compact Raman Spectrometer, Renishaw, UK). Microstructural and morphological investigations were conducted utilizing high-resolution field-emission scanning electron microscopy (HR-FESEM, GEMINI 300, Carl Zeiss, 15 kV). A BET surface area analyzer (Autosorb IQ-XR-XR, Anton Paar, Austria) was utilized to determine the specific surface area (S_{BET}) and pore size distribution curves.

2.4 Electrochemical measurement

The electrochemical characteristics of the electrode materials were investigated using an electrochemical workstation (CHI 660E) with a three-electrode setup. The prepared electrode, Ag/AgCl, and the Pt foil electrodes were used as the working electrode, the reference electrode, and the counter electrode, respectively, in a 6 M KOH electrolyte. The development of the working electrode was accomplished by combining the constituents in a weight ratio of 80 : 15 : 5. PCCuO nanocomposite, PVDF, and activated charcoal were dissolved in NMP as a solvent. After a thorough and comprehensive blending process, the resulting mixture was applied onto a stainless-steel strip and dried in a vacuum oven at 50 °C for 6 h to remove the solvent *via* evaporation.[39]

A symmetric supercapacitor device was assembled utilizing PCCuO-0.25 as both the negative and positive electrodes; the

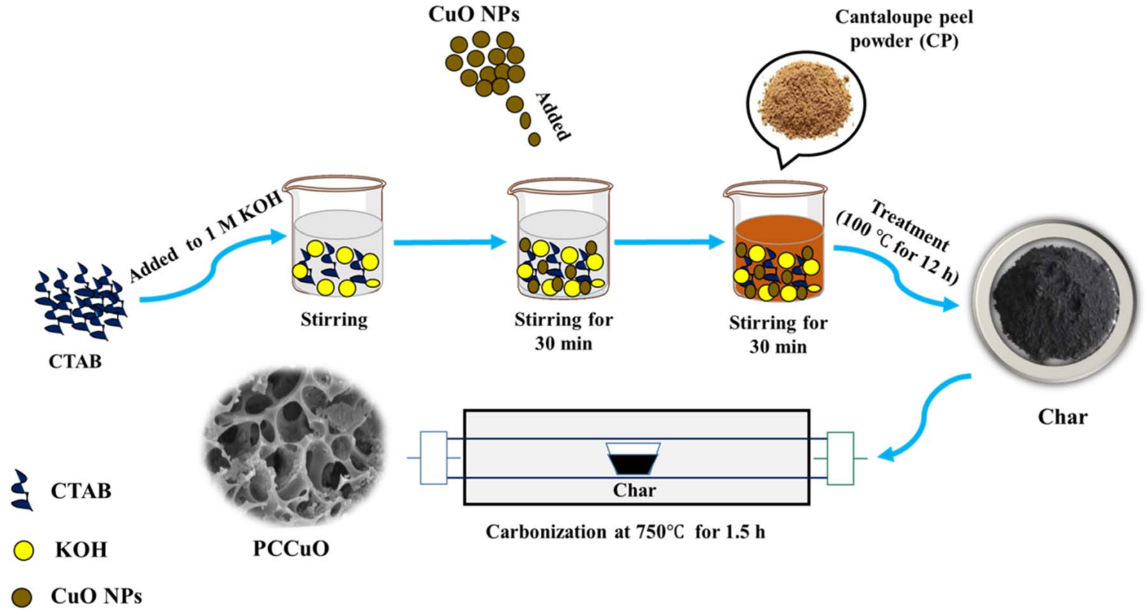

Scheme 1 Schematic of the synthesis process of the PCCuO nanocomposite through a one-step carbonization and activation method.

total mass of the active materials in both electrodes is 2.6 mg cm^{-2}. A 25 µm-thick Whatman 93 filter paper served as the separator, and a PVA/KOH gel was used as the electrolyte. The PVA/KOH gel electrolyte was prepared separately by dispersing 3 g of PVA and 2 g of KOH in 40 mL of DW and continuously stirring for 30 min prior to mix and heating at 60 °C for a duration of 1 h.[40]

The performance of the electrode was analyzed by the following electrochemical characterization techniques: cyclic voltammetry (CV), galvanostatic charge–discharge (GCD), and electrochemical impedance spectroscopy (EIS). The specific capacitance (C_{sp}) was calculated from the CV curves using the following equation:

$$C_{sp} = \frac{\int I\mathrm{d}V}{\varphi \cdot m\Delta V}\left(\mathrm{F\ g^{-1}}\right) \tag{1}$$

The galvanostatic charge–discharge curves can be used to calculate the C_{sp} according to the following equation:

$$C_{sp} = \frac{I \times \Delta t}{m \times \Delta V}\left(\mathrm{F\ g^{-1}}\right) \tag{2}$$

where I (A) represents the current during both charging and discharging operations, while the quantity of active electrode material is denoted as "m" (g). The scan rate, denoted as φ (V s^{-1}), and the change in potential represented by ΔV, is measured in volts, and the discharge time is denoted as "Δt" (s).

The coulombic efficiency (η) of the SCs was determined using the following equation:

$$\eta = \frac{\Delta t_d}{\Delta t_c} \tag{3}$$

where Δt_d and Δt_c denote the time of discharge and charge, respectively.

The practical application of SCs is determined by two critical factors: energy density (ED) and power density (PD), which can be calculated using the following equations:

$$\mathrm{ED} = \frac{C_{sp} \times \Delta V^2}{7.2}\left(\mathrm{Wh\ kg^{-1}}\right) \tag{4}$$

and

$$\mathrm{PD} = \frac{3600 \times E}{\Delta\ t}\left(\mathrm{W\ kg^{-1}}\right) \tag{5}$$

3 Results and discussion

Scheme 1 illustrates the synthesis process of a 3D-interconnected macroporous carbon–copper oxide (PCCuO) electrode *via* a single-step carbonization–activation method. First, CTAB was added to 1 M KOH under magnetic stirring. Then, CuO nanoparticles were added to the above solution under stirring to form a uniform solution. Next, cantaloupe peel powder was dispersed in the above mixture under stirring, followed by heating in a microwave oven. Subsequently, the resulting mixture was subjected to carbonization in a tubular furnace at 750 °C for a duration of 1.5 h under a N_2 atmosphere. In this case, cantaloupe fruit peels serve as sustainable precursors, rich in cellulose, hemicellulose, lignin, and residual carbohydrates.[41] These elements are vital because cellulose and hemicellulose provide the carbon backbone, and lignin contributes to thermal stability during carbonization–activation. During this process, KOH reacts with the carbon matrix, promoting pore development through redox reactions that generate mesopores and macropores. The lignin is also very high, which leads to the development of a strong aromatic-based carbon structure.

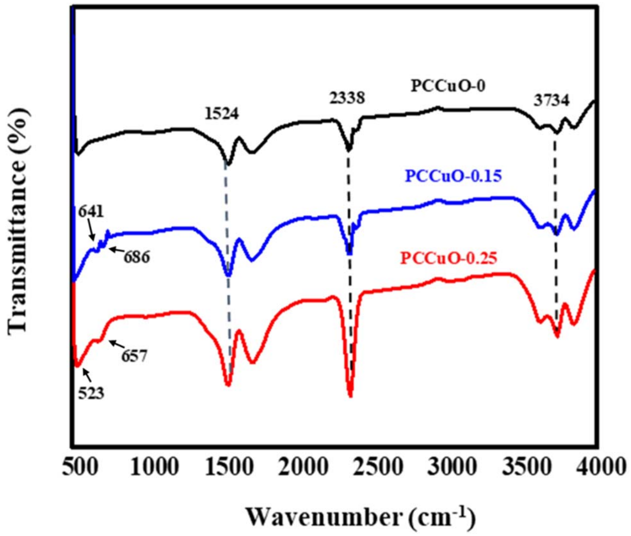

Fig. 1 FT-IR spectra of PCCuO-0, PCCuO-0.15, and PCCuO-0.25.

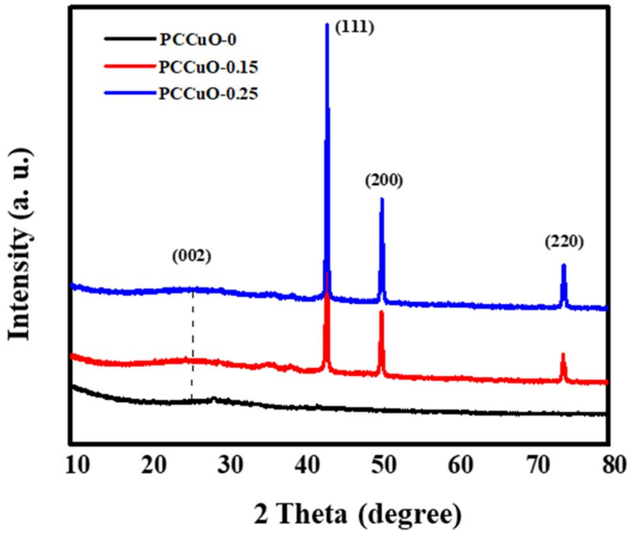

Fig. 2 XRD patterns of the PCCuO-0, PCCuO-0.15, and PCCuO-0.25 nanocomposites.

3.1 FT-IR analysis

FT-IR spectroscopy was employed to investigate the chemical composition and structural characteristics of the nanocomposite samples. Fig. 1 shows the FT-IR spectra of PCCuO-0, PCCuO-0.15, and PCCuO-0.25 nanocomposites. The pure PCCuO-0 sample exhibits a band at 1524 cm^{-1}, corresponding to C=C stretching vibrations, indicating the existence of an aromatic group, but the band located at 3734 cm^{-1} is related to the stretching of the O–H bond.[42] A strong peak observed at 2338 cm^{-1} is associated with interactions between the activated carbon and carbon dioxide molecules present in the atmosphere.[43] For the PCCuO-0.15 nanocomposite, the presence of three distinct peaks at 3733, 2336, and 1524 cm^{-1} corresponds to the O–H, CO_2, and C=C bonds of the porous carbon, respectively. Additionally, weak bands at 641 and 686 cm^{-1} are attributed to the stretching vibration of Cu–O.[44] The low intensity peak of the Cu–O peaks may be attributed to the limited quantity of CuO nanoparticles in PCCuO-0.15. The PCCuO-0.25 nanocomposite shows increased intensities of oxygen-containing functional groups and the appearance of new CuO peaks at 657 and 523 cm^{-1}. Moreover, the presence of the vibration mode of CuO nanoparticles at 523 and 657 cm^{-1}

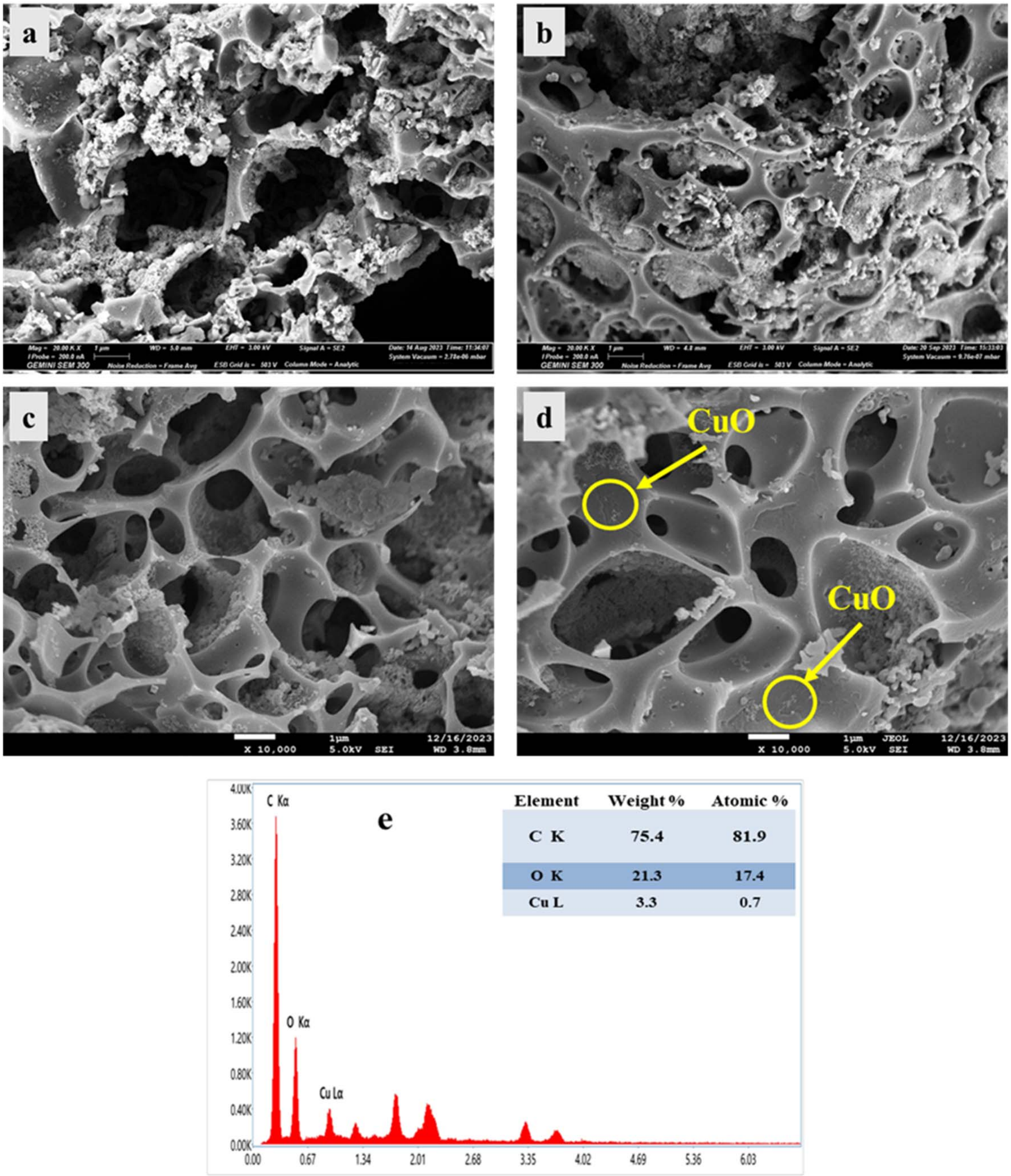

Element	Weight %	Atomic %
C K	75.4	81.9
O K	21.3	17.4
Cu L	3.3	0.7

Fig. 3 HR-FESEM images of (a) PCCuO-0, (b) PCCuO-0.15, (c and d) PCCuO-0.25 and (e) EDS analysis of the PCCuO-0.25 nanocomposite.

suggests the occurrence of bond stretching, bond formation, and vibrations between the nanocomposite components as residual oxygen-containing functional groups are replaced by CuO nanoparticles.[33] FT-IR analysis provides evidence of effective chemical interactions and changes in the porous carbon–CuO nanocomposite.

3.2 XRD analysis

Fig. 2 illustrates the XRD patterns of PCCuO-0, PCCuO-0.15, and PCCuO-0.25 nanocomposites. PCCuO-0 exhibits a diffraction peak at $2\theta = 26°$, which represents the (002) plane of graphitic carbon and evidences the presence of a graphitic phase within the porous carbon during the carbonization process.[21] The XRD pattern of PCCuO-0.15 shows distinct sharp peaks at $2\theta = 43.4°$, 50.4°, and 74°, which are ascribed to the (111), (200), and (220) crystallographic planes of Cu, respectively. These results are consistent with the Cu reference pattern (JCP-DS no. 04-0836).[24] The presence of a high concentration of copper species resulted in an increase in the intensity of Cu peaks in the case of PCCuO-0.15 and PCCuO-0.25 nanocomposites. The presence of Cu can be attributed to the incomplete reduction of copper oxide by carbon, whereas the possible incorporation of copper in PCCuO-0.15 and PCCuO-0.25 could potentially result in an additional decrease in the electrical resistance of the nanocomposite.

3.3 Morphological analysis

The surface morphologies of the PCCuO-0, PCCuO-0.15, and PCCuO-0.25 nanocomposites were investigated through HR-FESEM image analysis. Fig. 3(a) shows the HR-FESEM image of PCCuO-0 in the absence of copper oxide. The image reveals the presence of many macropores with diameters ranging from several hundred nanometers to several micrometers, which serve as an ion-buffering reservoir for electrolyte ion transport and enable rapid diffusion of electrolyte ions into the inner micropores of electrode materials, particularly at increased charging rates.[45] Moreover, some granules are observed on the surface of the porous carbon. The presence of granules is due to the thermal decomposition of organic precursors that leads to diverse pore structures.[46] Fig. 3(b) shows the HR-FESEM image of PCCuO-0.15, which reveals a rough and porous structure. Additionally, the effective dispersion of CuO nanoparticles residing on the surface of the porous medium is observed. Furthermore, compared to the bare PCCuO-0 support, the PCCuO-0.15 nanocomposite demonstrates a decreased volume of internal pores due to the presence of CuO species. After increasing the CuO concentration, PCCuO-0.25 shows well-dispersed CuO nanoparticles along the walls of the pore as a result of a 3D-interconnected hierarchical porous structure, as shown in Fig. 3(c and d). Additionally, Fig. 3(e) shows the EDS spectrum, confirming the presence of carbon (75.4 wt%), oxygen (21.3 wt%), and copper (3.3 wt%), which ensures the successful deposition of copper oxide onto the 3D porous network structure.

3.4 Raman spectroscopy studies

Raman spectroscopy was employed to obtain information about the degree of graphitization and the presence of defects in the PCCuO-0, PCCuO-0.15, and PCCuO-0.25 nanocomposites, as depicted in Fig. 4. Two main peaks observed at 1356 and 1588 cm^{-1} represent the D-band and G-band of graphitic carbon, respectively. The D-band is associated with the presence of defects in the graphite structure, while the G-band is associated with the sp^2-hybridized carbon atoms.[47] The intensity ratio of the D-band to the G-band (I_D/I_G) can be used to estimate the degree of disorder in the carbon material.[48]

The I_D/I_G values of PCCuO-0.25, PCCuO-0.15, and PCCuO-0 are 0.92, 0.83, and 0.81, respectively. A small I_D/I_G value indicates a higher degree of graphitization and fewer defects in the carbon structure, which may be due to the catalytic graphitization effect of CuO on carbon. This suggests that the carbon network is well-ordered, which enhances electrical conductivity and electrochemical performance. A lower I_D/I_G ratio implies that CuO has been effectively added to the porous carbon.

3.5 BET analysis

N_2 adsorption–desorption curves were conducted to determine the surface area and pore size distribution of PCCuO-0, PCCuO-0.15, and PCCuO-0.25, as depicted in Fig. 5. The pure carbon and nanocomposites exhibit type IV isotherms with a hysteresis loop at $P/P_o = 0.45–1$, indicating that they have high porosity with hierarchical mesopore-dominated structures (Fig. 5(a)) .[49] The presence of a large number of microporous structures is clearly noticed in the substantial absorption of nitrogen in the samples at a P/P_o ratio of less than 0.05. When the relative pressure is near 1, the significantly increased adsorption amount suggests the existence of macropores, which facilitate electrolyte transport and charge transfer during the charging and discharging process.[32] The pore size distribution depicted

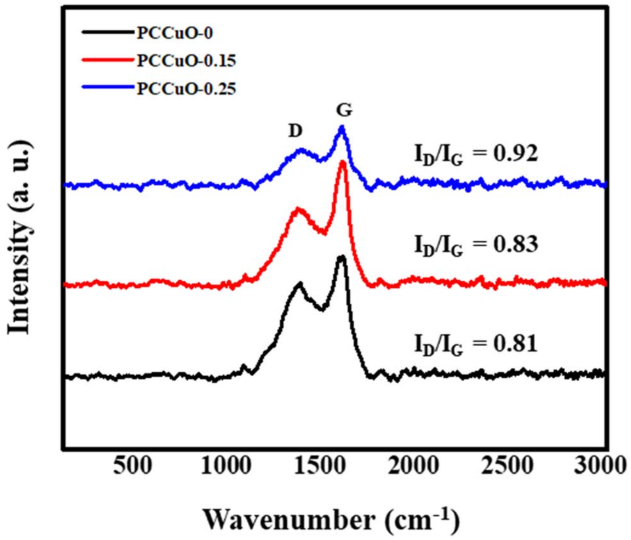

Fig. 4 Raman spectra of the PCCuO-0, PCCuO-0.15, and PCCuO-0.25 nanocomposites.

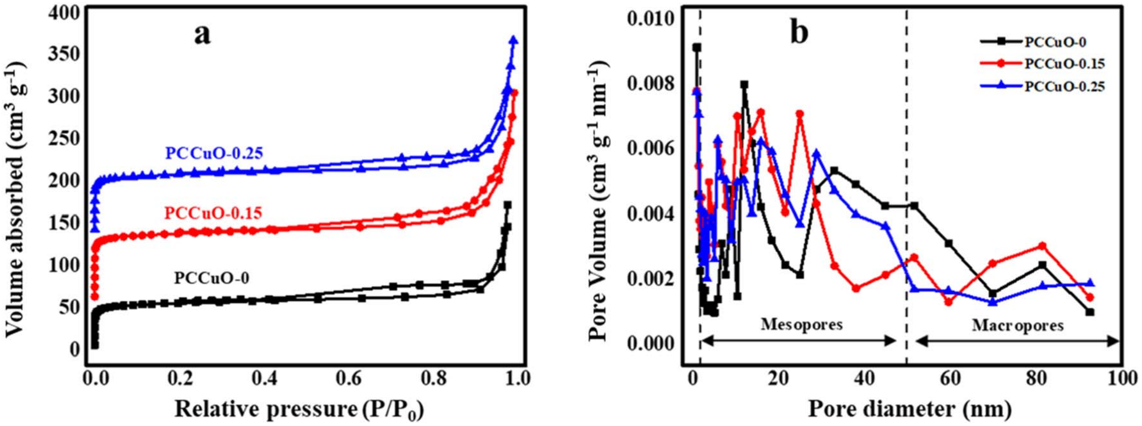

Fig. 5 (a) N_2 adsorption/desorption isotherms and (b) pore size distribution curves of the nanocomposites.

in Fig. 5(b) provides further affirmation that PCCuO-0, PCCuO-0.15, and PCCuO-0.25 exhibit a 3D-interconnected porous structure comprising both micropores and mesopores. Table 1 indicates that more porosity is present in the nanocomposite due to KOH activation, which allows for more effective carbonization and generates a rich pore structure. PCCuO-0 shows a small specific surface area of 202.8 m^2 g^{-1} and a large pore volume of 0.3332 cm^3 g^{-1}. However, the PCCuO-0.15 and PCCuO-0.25 nanocomposites demonstrate specific surface areas of 269.75 m^2 g^{-1} and 307.29 m^2 g^{-1}, respectively, and pore volumes of 0.3209 cm^3 g^{-1} and 0.3261 cm^3 g^{-1}. The surface area of the composite material was greatly increased by the addition of CuO to bare PCCuO-0. The increased surface area of PCCuO-0.15 and PCCuO-0.25 with mesopores is anticipated to improve electrochemical performance. Additionally, the average pore diameter of PCCuO-0.25 is 10.5 nm. Therefore, PCCuO-0.25 demonstrates a suitable porous structure and a wide specific surface area, which makes it easier to increase the specific capacity.

3.6 Electrochemical performance of PCCuO-0, PCCuO-0.15, and PCCuO-0.25 electrodes

The electrochemical performance of the synthesized PCCuO-0, PCCuO-0.15, and PCCuO-0.25 electrode materials was evaluated with a CV test in a three-electrode setup using 6 M KOH as the electrolyte at ambient temperature. As shown in Fig. 6(a), the CV curves of the electrodes were recorded at a scan rate of 10 mV s^{-1} within a potential range of −0.3 to +0.3 V. The CV curve of the PCCuO-0 electrode exhibits a quasi-rectangular shape owing to both the double-layer behavior of porous carbon and the pseudocapacitance due to the presence of oxygen functionalities.[50] Furthermore, the CV curves of PCCuO-0.15 and PCCuO-0.25 electrodes exhibit nearly rectangular shapes with small redox peaks, indicating hybrid capacitor characteristics resulting from the combination of the electric double-layer capacitance of porous carbon and the pseudocapacitance of CuO. The mechanism of reversible redox reactions of electrodes can be explained as follows:

$$CuO + H_2O + OH^- \leftrightarrow CuOOH + e^- \tag{6}$$

$$Cu + H_2O + 2OH^- \leftrightarrow CuOOH + 2e^- \tag{7}$$

Table 1 Summary of the structural characteristics of the nanocomposites

Samples	Specific surface area (m^2 g^{-1})	Pore volume (cm^3 g^{-1})	Average pore diameter (nm)
PCCuO-0	202.8	0.3332	15.7
PCCuO-0.15	269.75	0.3209	10.02
PCCuO-0.25	307.29	0.3261	10.5

As estimated, the integrated CV area of the PCCuO-0.25 electrode is considerably larger than that of the PCCO-0.15 and PCCuO-0 electrodes, indicating that the PCCuO-0.25 electrode had a substantially higher specific capacitance than the PCCuO-0.15 and PCCuO-0 electrodes. The CV curves of PCCuO-0, PCCuO-0.15 and PCCuO-0.25 electrodes at scan rates ranging from 10 to 50 mV s^{-1} are comparatively illustrated in Fig. 6(b–d). As predicted, the PCCuO-0, PCCuO-0.15, and PCCuO-0.25 electrodes exhibit larger CV curves with increasing scanning rates. In addition, the intensities of the peak currents rose with the escalation of the scan rates, which is attributable to the polarization effect of the electrode.[51]

The specific capacitance (C_{sp}) was calculated using eqn (1). The C_{sp} values were obtained as 297, 362.3, and 457.2 F g^{-1} for PCCuO-0, PCCuO-0.15, and PCCuO-0.25 electrodes, respectively, at a scan rate of 10 mV s^{-1}. These results suggest that PCCuO-0.25 demonstrates superior electrochemical characteristics in comparison to PCCuO-0.15 and PCCuO-0 due to the presence of an interconnected macroporous network in the 3D carbon structure. This network enhances surface utilization efficiency, decreases ion and mass transport distances, and improves accessibility to active sites. Furthermore, the carbon-based porous material benefits from the synergistic effects of the highly conductive Cu metal and highly capacitive CuO.[52]

The observed results clearly show that C_{sp} decreases as the scan rate increases, as shown in Fig. 6(e). This phenomenon can

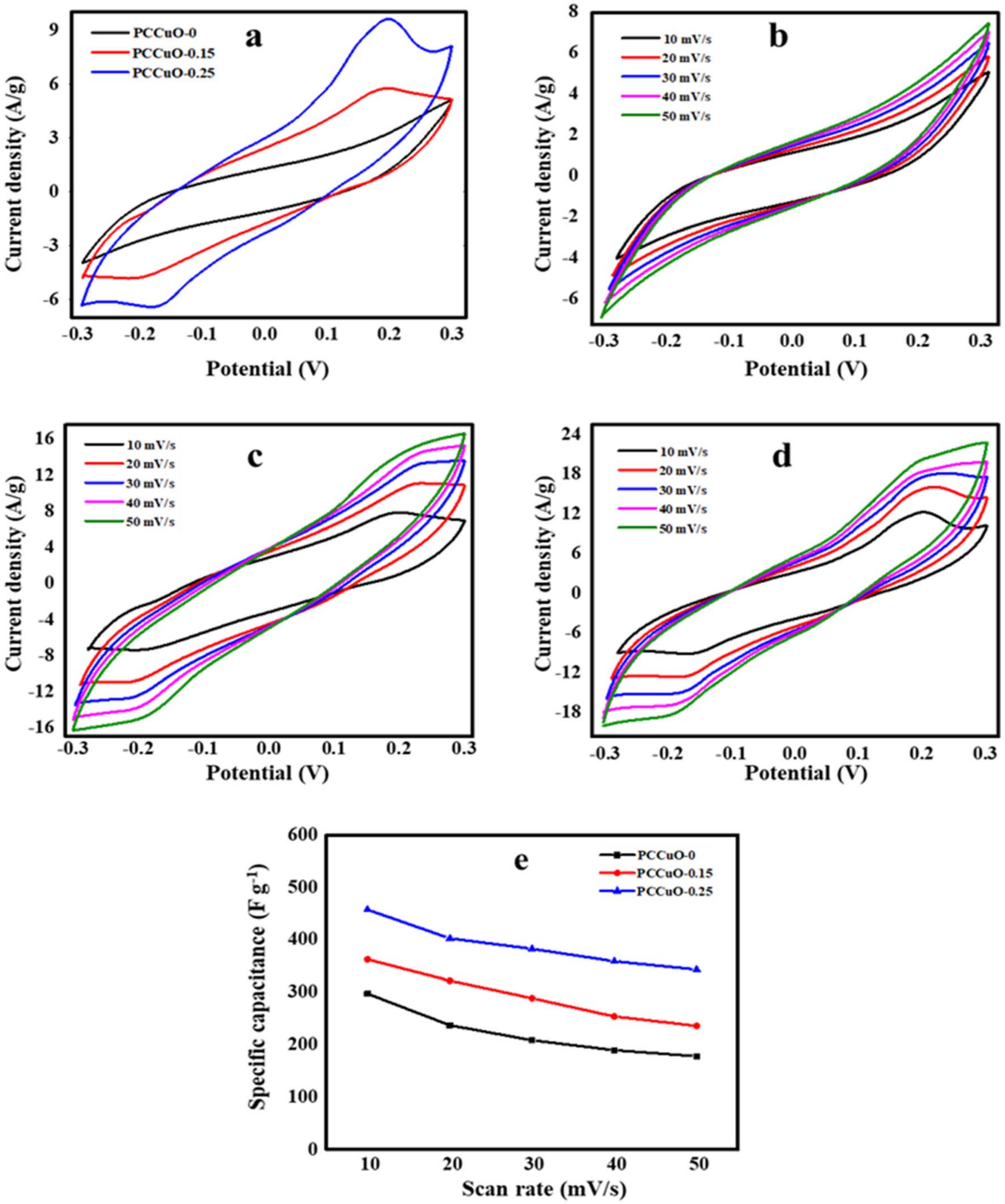

Fig. 6 (a) CV curves of PCCuO-0, PCCuO-0.15 and PCCuO-0.25 electrodes at a scan rate of 10 mV s^{-1}; CV curves of (b) PCCuO-0, (c) PCCuO-0.15, and (d) PCCuO-0.25 at scan rates from 10 to 50 mV $^{-1}$s; and (e) variation of specific capacitance with different scan rates from 10 to 50 mV s^{-1}.

be attributed to the fact that a reduced scan rate could not allow the electrochemical process to proceed effectively. Consequently, only the interface of the active substance *e* would effectively participate in generating the observed capacitance.[20] In addition, the CV curves of PCCuO-0.25 exhibit a similar shape even at a scan rate of 50 mVs^{-1}, indicating fast ion transportation between the electrode and electrolyte interface due to the 3D network structure and possibly the short diffusion paths of the porous carbon.

The galvanostatic charge–discharge (GCD) behavior of PCCuO-0, PCCuO-0.15, and PCCuO-0.25 electrodes is shown in Fig. 7(a–c) at various current densities ranging from 1.5 to 3 A g^{-1} at a fixed potential window of −0.3 to 0.3 V. The charge–discharge curves of all samples demonstrate a quasi-triangular shape within the potential range of −0.3 to 0.3 V; this suggests that there is significant involvement of double-layer capacitance with a minor contribution from pseudocapacitance. The pseudocapacitive phenomenon of PCCuO samples may arise

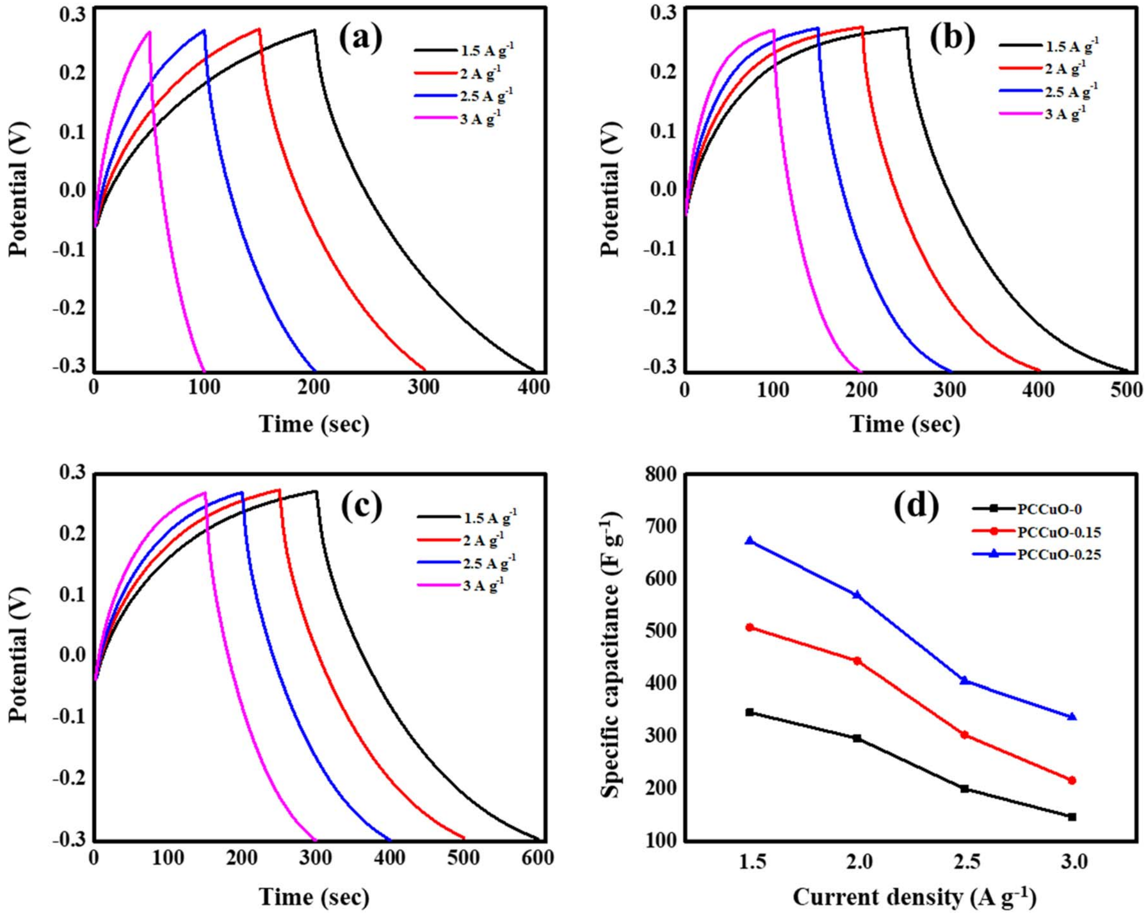

Fig. 7 GCD curves for the (a) PCCuO-0, (b) PCCuO-0.15, and (c) PCCuO-0.25 nanocomposites at varying current densities from 1.5 to 3 A g^{-1}; and (d) variation of specific capacitance with CD.

from the existence of oxygen moieties in the porous carbon and the incorporation of CuO nanoparticles, which significantly enhance the wetting capability of the electrode surface and increase the number of electrochemically active sites.[53] The C_{sp} was calculated using eqn (2), and the obtained C_{sp} for PCCuO-0.25 is 673 F g^{-1} at a current density of 1.5 A g^{-1}. These values are significantly higher than those of PCCuO-0.15 (507.5 F g^{-1}) and PCCuO-0 (345.4 F g^{-1}), as illustrated in Fig. 7(a–c) and listed in Table 2. The high specific capacitance of the PCCuO-0.25 electrode is ascribed to (i) its extensive macroporous structure, which facilitates the reduction of the diffusion distance from the external electrolytes to the internal surfaces; (ii) the presence of Cu, which offers a highly conductive framework that enhances the electrical conductivity of the composite; and (iii) the involvement of CuO in the redox

Table 2 Specific capacitance of PCCuO nanocomposites calculated from the GCD test at different current densities

Current density (A g^{-1})1	Specific capacitance (F g^{-1})		
	PCCuO-0	PCCuO-0.15	PCCuO-0.25
1.5	345.4	507.5	673
2	296	443.2	548.2
2.5	200	302.6	405
3	146.7	216	336

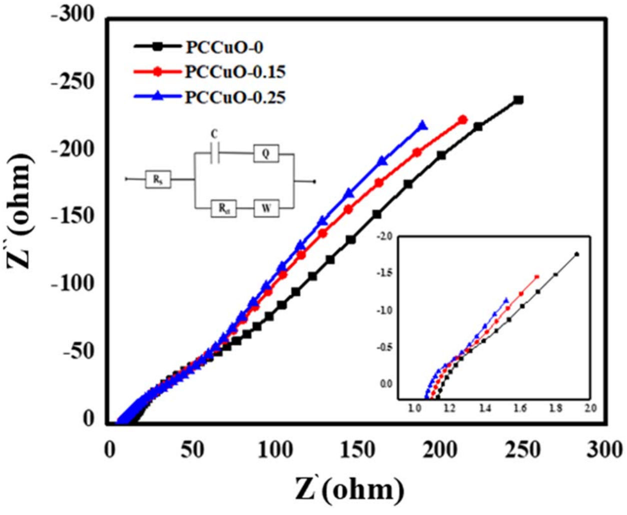

Fig. 8 Nyquist plots and an equivalent circuit (inset) of the PCCuO-0, PCCuO-0.15, and PCCuO-0.25.

Table 3 Fitted electronic components using the Randle equivalent circuit model

Materials	R_S (Ω)	R_{ct} (Ω cm^2)	C (F)
PCCuO-0	2.87	4.53	5.255×10^{-5}
PCCuO-0.15	2.02	2.9	9.215×10^{-5}
PCCuO-0.25	1.72	1.58	7.430×10^{-5}

reaction, which contributes to pseudocapacitance. As shown in Fig. 7(d), the specific capacitance of electrodes based on PCCuO demonstrates a decrease as the current density increases. This observation is due to the collaborative effects of pseudocapacitance from CuO nanoparticles and double-layer capacitance of the porous carbon material. However, electrolyte ions are unable to participate in the redox reaction promptly when exposed to high current densities. As a result, there is a significant decrease in the specific capacitance.[32]

3.7 Electrochemical impedance spectroscopy analysis

The electrochemical impedance characteristics of PCCuO-0, PCCuO-0.15, and PCCuO-0.25 nanocomposites were measured over a frequency range of 0.1 Hz to 100 kHz, as demonstrated in Fig. 8. The Nyquist plot comprises two regions: (a) a semicircular section at high frequencies that delimits the charge transfer resistance, and (b) a linear segment located in the lower frequency range, which is associated with the diffusion-limited process occurring during electrochemical charge accumulation.[54] Compared with PCCuO-0, the linear part of PCCuO-0.25 is more vertical, indicating a behavior closer to that of an ideal capacitor. The diameter of the semi-circular region at high frequency signifies the charge transfer resistance (R_{ct}), which is associated with the interface between the electrode material/electrolyte and the current collector.[55] The Randle equivalent circuit model was used to analyze the EIS data obtained, as depicted in the inset of Fig. 8. The electronic parameters of the equivalent circuit model involve the solution resistance (R_s), charge transfer resistance (R_{ct}), the capacitance (C), Warburg diffusion impedance (W), and constant phase element (Q). Table 3 provides a succinct summary of the fitted parameters. The three devices exhibit low internal resistance of the electrode materials and good electrical conductivity of the electrolyte. For PCCuO-0, PCCuO-0.15, and PCCuO-0.25, the fitted R_{ct} values are 4.53, 2.9, and 1.58 Ω.cm^2, respectively. It is noteworthy that the PCCuO-0.25 nanocomposite has the lowest R_{ct} when compared to PCCuO-0 and PCCuO-0.25. Additionally, a lower R_{ct} value also suggests a faster charge transfer at the electrode–electrolyte interfaces and higher ionic conductivity in

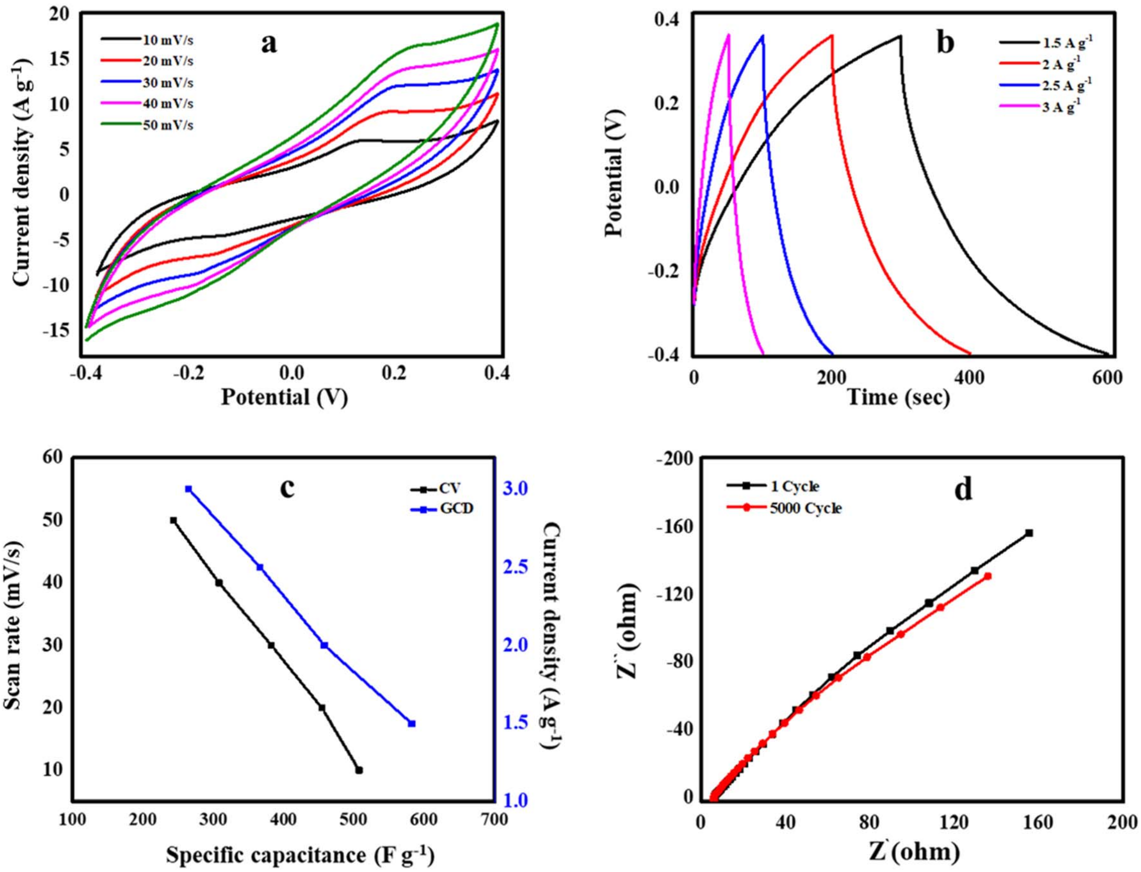

Fig. 9 (a) CV curve of the PCCuO-0.25 SSC device at various scan rates, (b) GCD curve of the PCCuO-0.25 SSC device at various CDs, (c) comparison of C_{sp} at different scan rates and CDs for CV and GCD, respectively, and (d) Nyquist plots of the PCCuO-0.25 SSC device for the 1st and 5,000th cycles.

the electrolyte. This suggests that the PCCuO-0.25 electrode has better pore accessibility to the ions of the electrolyte, which leads to higher capacitance values.

3.8 Electrochemical properties of PCCuO-0.25 symmetric supercapacitor

To examine the electrochemical performance of the PCCO-0.25 material for practical applications, a solid-state SSC was assembled using two PCCuO-0.25 electrodes with a PVA/KOH gel as the electrolyte. The electrochemical characteristics of the PCCuO-0.25//PCCuO-0.25 SSC were examined *via* a two-electrode setup utilizing CV, GCD, and EIS, as illustrated in Fig. 9. The CV profiles of the PCCuO-0.25 SSC at different scan rates, in the potential range of −0.4 to +0.4 V, are illustrated in Fig. 9(a). All CV profiles have quasi-rectangular shapes at scan rates from 10 to 50 mV s^{-1}, indicating the Faradic-type behavior and rapid ion transfer of the symmetric EDLCs due to the 3D-interconnected porous structure, which facilitates rapid ionic motion.

The GCD curves of the PCCuO-0.25//PCCuO-0.25 SSC at various current densities from 1.5 to 3 A g^{-1} are shown in Fig. 9(b). The GCD curves exhibit a quasi-triangular form with minimal voltage drops at varying current densities from 1.5 to 3 A g^{-1}, signifying low equivalent series resistance and outstanding electrochemical reversibility.[56] The discharge time increases as the current density decreases, owing to the limitations in charge transport and ion diffusion coefficients at rising current densities. The specific capacitance of the PCCuO-0.25//PCCuO-0.25 SSC device, derived from the GCD curve, is 582 F g^{-1} at a current density of 1.5 A g^{-1}, and it retains 264.4 F g^{-1} at a higher current density of 3 A g^{-1}. Fig. 9(c) depicts the plot of specific capacitance *vs.* scan rates and current densities, generated from CV and GCD, respectively. When scan rates and current density increase, the specific capacitance decreases, indicating that the active materials cannot respond quickly enough to the applied current. This is indicative of inadequate redox activity that reduces the operation of the supercapacitor at high rates.[57]

The Nyquist plot of the PCCO-0.25//PCCuO-0.25 SSC device is shown in Fig. 9(d). In the low-frequency region, an increase in impedance is represented, which indicates the high efficiency of the PCCuO-0.25//PCCuO-0.25 SSC device. However, a slight shift in the Nyquist plot of the PCCuO-0.25//PCCuO-0.25 SSC device after 5000 cycles shows that the PCCuO-0.25//PCCuO-0.25 SSC device has very good cycle stability and moderate performance.

Fig. 10(a) shows the linear correlation between log current density (I_p) and log scan rate (mV). According to the power–law

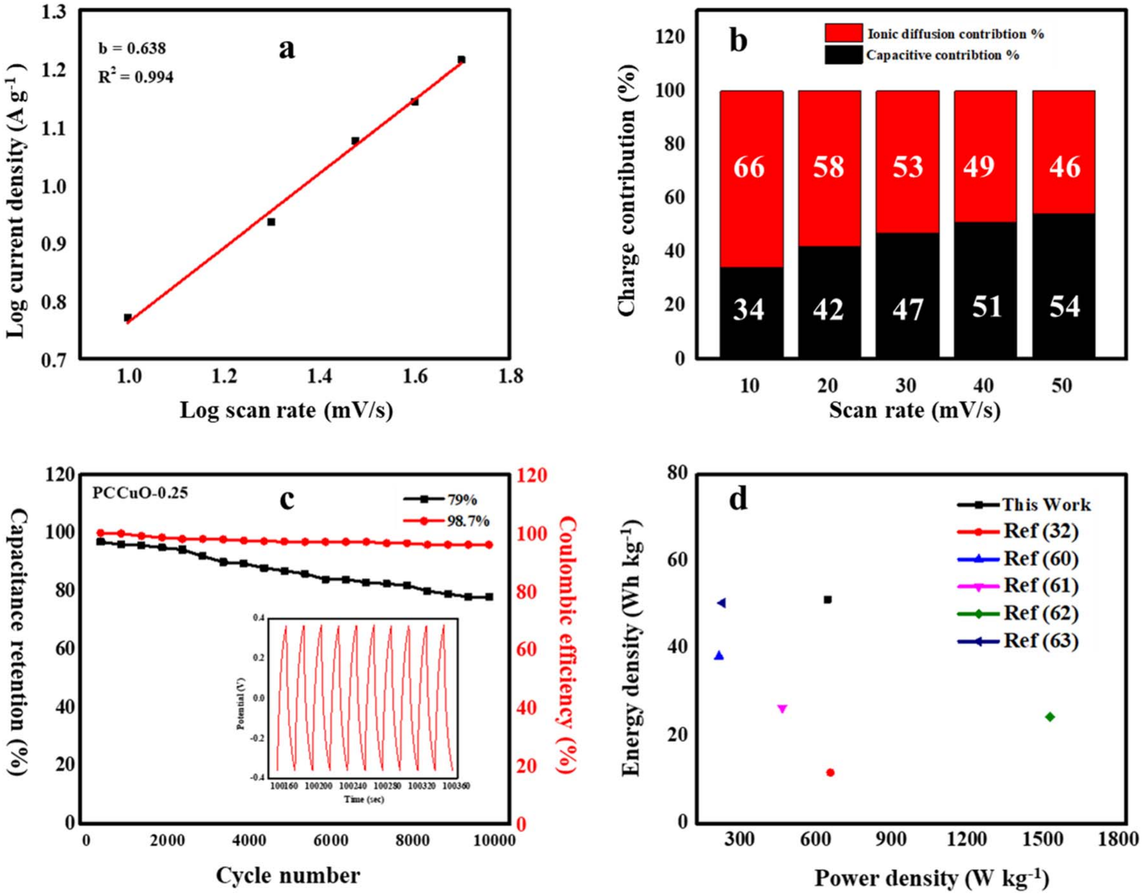

Fig. 10 (a) log(I_p) *vs.* log(v) plot; (b) charge contribution of the PCCO-0.25//PCCuO-0.25 SSC; (c) the capacitance retention and coulombic efficiency of the PCCuO-0.25//PCCuO-0.25 SSC at a CD of 3 A g^{-1} (inset: the last 10 cycles of the GCD curve); and (d) comparison of the energy densities of the PCCuO-0.25//PCCuO-0.25 SSC with the previous works.

Table 4 Comparison of the performance of this study with recent research on porous carbon and copper oxide nanocomposites

Samples	CD ($A\ g^{-1}$)	C_{sp} ($F\ g^{-1}$)	ED ($Wh\ kg^{-1}$)	PD ($W\ kg^{-1}$)	Ref.
CuO-AC	1	530	11.7	628.73	32
CuO/rGO@NF	—	—	38.35	187.5	60
CuO-MPC//AC	1	98	26.6	438	61
Cu/PCNFs	1	333.5	24.53	1500	62
CuO-NW/RGO	1	364	50.6	200	63
PCCuO-0.25//PCCuO-0.25	1.5	582	51.4	616.8	This work

equation ($I_p = av^b$), the mean value of b is determined by the slope of the log(mV) *vs.* log(I_p) curve, whereas the value of a remains constant. The properties of controlled diffusion are shown by the parameter b, which is 0.5, while capacitive behaviour is indicated by a value of 1. The PCCuO-0.25 electrode material exhibited a slope value of $b = 0.63$. It is significant to note the rapid reversible redox reaction due to Cu^{2+} ions, which confirms diffusion-controlled behaviour. In Fig. 10(b), the bar graph depicts both the capacitive and ion diffusion charge contributions at different scan rates, as determined by the Dunn's method. The ion-diffusion charge contribution reaches 66, 58, 53, 49, and 46%, while the capacitive charge contribution ranges from 34, 42, 47, 51, and 54%, respectively. As the scan speed increases, the participation of Cu^{2+} ions greatly enhances the pseudocapacitive charge contribution. The contribution of ion-diffusion charge and capacitive charge is dependent on the scan rate.

Cyclic stability is an important factor in evaluating the long-term reliability and performance of supercapacitors. Consequently, the PCCuO-0.25//PCCuO-0.25 SSC device exhibits long cycling stability and improved energy storage capabilities. Fig. 10(c) depicts the specific capacitance *versus* cycle number of the PCCuO-0.25//PCCuO-0.25 SSC device at a current density of 3 A g^{-1}. The specific capacitance is slightly decreased after 3000 cycles. However, it retains up to 10 000 cycles. After 10 000 cycles, the PCCuO-0.25//PCCuO-0.25 SSC device retains 79% of its initial specific capacitance. The coulombic efficiency (η) was determined *via* a charge–discharge process, computed from eqn (3). The coulombic efficiency is recorded at 98.7%, as depicted in Fig. 10(c). This high efficiency is due to the reversible nature of the electrostatic charge storage mechanism. During discharge, charges are released, resulting in minimal energy losses and high coulombic efficiency. In addition, the high stability of the PCCuO-0.25//PCCuO-0.25 SSC arises from the collaborative impact of CuO nanoparticles and porous carbon. On the other hand, the deposition of CuO nanoparticles on porous carbon effectively reduces the diffusion and migration distance of electrolyte ions during the fast electrochemical process.[58] Conversely, porous carbon demonstrates exceptional conductivity for PCCuO-0.25 composites within the electrode, resulting in enhanced electrochemical stability.[59]

The energy densities of the constructed supercapacitor at different power densities were determined using eqn (4) and (5), as shown in Fig. 10(d). The SSC system exhibits a high energy density of 51.4Wh kg^{-1} at a maximum power density of 616.8 W kg^{-1}, surpassing the majority of previously documented results, such as CuO-AC (11.7 Wh kg^{-1}, 628.73 W kg^{-1}),[32] CuO/rGO@NF (38.35 Wh kg^{-1}, 187.5 W kg^{-1}),[60] CuO/MPC (26.6 Wh kg^{-1}, 438 W kg^{-1}),[61] Cu/PCNFs (24.53 Wh kg^{-1}, 1500 W kg^{-1}),[62] CuO-NW/RGO (50.6 Wh kg^{-1}, 200 W kg^{-1}),[63] as shown in Table 4.

4 Conclusions

Herein, a 3D-interconnected porous carbon material was derived from cantaloupe peel and copper oxide nanocomposite (PCCuO) using a one-step carbonization–activation method. Structural and morphological studies show a clear 3D-interconnected hierarchical porous structure with uniformly dispersed copper oxide nanoparticles. The PCCuO-0.25 nanocomposite demonstrates a significantly high specific capacitance of 673 F g^{-1}, which is much higher than that of PCCuO-0.15 (507.5 F g^{-1}) and pure PCCuO-0 (345.4 F g^{-1}) at a current density of 1.5 A g^{-1}, measured using a three-electrode setup. When the PCCuO-0.25 composite material is employed as both the positive and negative electrodes in a symmetric supercapacitor, it delivers a high ED of 51.4 Wh kg^{-1} at PD of 616.8 W kg^{-1}, along with outstanding cycling stability with capacitance retention of 79% and a coulombic efficiency of 98.7% after 10 000 charging–discharging cycles. This study provides a development of energy storage devices with high energy density, superior rate performance, and exceptional cycle stability, leveraging redox in copper oxide and electric double-layer capacitance in carbon-based materials.

Conflicts of interest

There are no conflicts to declare.

Data availability

The authors confirm that all the data supporting findings of this study are available within the article.

Acknowledgements

Thanks to PURSE Lab for providing characterization facility. And also acknowledged to University of Aden [(310) 2021] for providing fellowship to my PhD programme.

References

1 L. Hu, Q. Zhu, Q. Wu, D. Li, Z. An and B. Xu, Natural Biomass-Derived Hierarchical Porous Carbon Synthesized by an *in Situ* Hard Template Coupled with NaOH Activation for Ultrahigh Rate Supercapacitors, *ACS Sustain. Chem. Eng.*, 2018, **6**(11), 13949–13959, DOI: 10.1021/acssuschemeng.8b02299.

2 Y. Shi, *et al.*, Porous Carbon with Willow-Leaf-Shaped Pores for High-Performance Supercapacitors, *ACS Appl. Mater. Interfaces*, 2017, **9**(49), 42699–42707, DOI: 10.1021/acsami.7b12776.

3 L. Xu, *et al.*, In situ growth of Cu2O/CuO nanosheets on cu coating carbon cloths as a binder-free electrode for asymmetric supercapacitors, *Front. Chem.*, 2019, **7**, 420, DOI: 10.3389/fchem.2019.00420.

4 S. Maji, *et al.*, High-Performance Supercapacitor Materials Based on Hierarchically Porous Carbons Derived from Artocarpus heterophyllus Seed, *ACS Appl. Energy Mater.*, 2021, **4**(11), 12257–12266, DOI: 10.1021/acsaem.1c02051.

5 P. Hao, *et al.*, Hierarchical porous carbon aerogel derived from bagasse for high performance supercapacitor electrode, *Nanoscale*, 2014, **6**(20), 12120–12129, DOI: 10.1039/c4nr03574g.

6 Q. Abbas, M. Mirzaeian, A. A. Ogwu, M. Mazur and D. Gibson, Effect of physical activation/surface functional groups on wettability and electrochemical performance of carbon/activated carbon aerogels based electrode materials for electrochemical capacitors, *Int. J. Hydrogen Energy*, 2020, **45**(25), 13586–13595, DOI: 10.1016/j.ijhydene.2018.04.099.

7 M. S. Ismail, M. D. Yahya, M. Auta and K. S. Obayomi, Facile preparation of amine -functionalized corn husk derived activated carbon for effective removal of selected heavy metals from battery recycling wastewater, *Heliyon*, 2022, **8**(5), e09516, DOI: 10.1016/j.heliyon.2022.e09516.

8 T. Ramesh, N. Rajalakshmi, K. S. Dhathathreyan and L. R. G. Reddy, Hierarchical Porous Carbon Microfibers Derived from Tamarind Seed Coat for High-Energy Supercapacitor Application, *ACS Omega*, 2018, **3**(10), 12832–12840, DOI: 10.1021/acsomega.8b01850.

9 A. Jain and S. K. Tripathi, Nano-porous activated carbon from sugarcane waste for supercapacitor application, *J. Energy Storage*, 2015, **4**, 121–127, DOI: 10.1016/j.est.2015.09.010.

10 N. Kanjana, *et al.*, Preparation of a hierarchical porous activated carbon derived from cantaloupe peel/fly ash/PEDOT:PSS composites as Pt-free counter electrodes of dye-sensitized solar cells, *Heliyon*, 2024, **10**(9), e29957, DOI: 10.1016/j.heliyon.2024.e29957.

11 N. Ahmad, *et al.*, Pre-treated biomass waste melon peels for high energy density semi solid-state supercapacitors, *J. Power Sources*, 2024, **624**, 235511, DOI: 10.1016/j.jpowsour.2024.235511.

12 K. Surya and M. S. Michael, Novel interconnected hierarchical porous carbon electrodes derived from bio-waste of corn husk for supercapacitor applications, *J. Electroanal. Chem.*, 2020, **878**, 114674, DOI: 10.1016/j.jelechem.2020.114674.

13 Y. Qin, *et al.*, Hydrogen-Bonded Interfacial Super-Assembly of Spherical Carbon Superstructures for High-Performance Zinc Hybrid Capacitors, *Nano-Micro Lett.*, 2026, **18**(1), 38, DOI: 10.1007/s40820-025-01883-1.

14 T. Shi, *et al.*, Hierarchical porous carbon guided by constructing organic-inorganic interpenetrating polymer networks to facilitate performance of zinc hybrid supercapacitors, *Chin. Chem. Lett.*, 2025, **36**(1), 109559, DOI: 10.1016/j.cclet.2024.109559.

15 L. Li, *et al.*, N/P Codoped Porous Carbon/One-Dimensional Hollow Tubular Carbon Heterojunction from Biomass Inherent Structure for Supercapacitors, *ACS Sustainable Chem. Eng.*, 2018, **7**(1), 1337–1346, DOI: 10.1021/acssuschemeng.8b05022.

16 K. Wang, Z. Zhang, Q. Sun, P. Wang and Y. Li, Durian shell-derived N, O, P-doped activated porous carbon materials and their electrochemical performance in supercapacitor, *J. Mater. Sci.*, 2020, **55**(23), 10142–10154, DOI: 10.1007/s10853-020-04740-1.

17 L. Ma, *et al.*, Synthesis of a Three-Dimensional Interconnected Oxygen-, Boron-, Nitrogen-, and Phosphorus Tetratomic-Doped Porous Carbon Network as Electrode Material for the Construction of a Superior Flexible Supercapacitor, *ACS Appl. Mater. Interfaces*, 2020, **12**(41), 46170–46180, DOI: 10.1021/acsami.0c13454.

18 X. Liu, C. Yu, Z. Chen, F. Xu, W. Liao and W. Zhong, Biomass Peach Gum-Derived Heteroatom-Doped Porous Carbon*via in Situ* Molten Salt Activation for High-Performance Supercapacitors, *Energy Fuels*, 2021, **35**(23), 19801–19810, DOI: 10.1021/acs.energyfuels.1c03064.

19 S. Sharma, M. Kaur, C. Sharma, A. Choudhary and S. Paul, Biomass-Derived Activated Carbon-Supported Copper Catalyst: An Efficient Heterogeneous Magnetic Catalyst for Base-Free Chan-Lam Coupling and Oxidations, *ACS Omega*, 2021, **6**(30), 19529–19545, DOI: 10.1021/acsomega.1c01830.

20 E. Elaiyappillai, *et al.*, Low cost activated carbon derived from Cucumis melo fruit peel for electrochemical supercapacitor application, *Appl. Surf. Sci.*, 2019, **486**, 527–538, DOI: 10.1016/j.apsusc.2019.05.004.

21 Q. Wang, Y. Zhang, J. Xiao, H. Jiang, T. Hu and C. Meng, Copper oxide/cuprous oxide/hierarchical porous biomass-derived carbon hybrid composites for high-performance supercapacitor electrode, *J. Alloys Compd.*, 2019, **782**, 1103–1113, DOI: 10.1016/j.jallcom.2018.12.235.

22 Y. Xi, Z. Xiao, H. Lv, H. Sun, S. Zhai and Q. An, Construction of CuO/Cu-nanoflowers loaded on chitosan-derived porous carbon for high energy density supercapacitors, *J. Colloid Interface Sci.*, 2023, **630**, 525–534, DOI: 10.1016/j.jcis.2022.10.037.

23 S. D. Dhas, *et al.*, Synthesis of NiO nanoparticles for supercapacitor application as an efficient electrode material, *Vacuum*, 2019, **181**, 109646, DOI: 10.1016/j.vacuum.2020.109646.

24 G. S. Jang, S. Ameen, M. S. Akhtar and H. S. Shin, Cobalt oxide nanocubes as electrode material for the performance evaluation of electrochemical supercapacitor, *Ceram. Int.*, 2018, **44**(1), 588–595, DOI: 10.1016/j.ceramint.2017.09.217.

25 P. S. Murphin Kumar, *et al.*, Green route synthesis of nanoporous copper oxide for efficient supercapacitor and capacitive deionization performances, *Int. J. Energy Res.*, 2020, **44**(13), 10682–10694, DOI: 10.1002/er.5712.

26 Y. Kumar, S. Chopra, A. Gupta, Y. Kumar, S. J. Uke and S. P. Mardikar, Low temperature synthesis of MnO2 nanostructures for supercapacitor application, *Mater. Sci. Energy Technol.*, 2020, **3**, 566–574, DOI: 10.1016/j.mset.2020.06.002.

27 M. S. Yadav, N. Singh and A. Kumar, Synthesis and characterization of zinc oxide nanoparticles and activated charcoal based nanocomposite for supercapacitor electrode application, *J. Mater. Sci. Mater. Electron.*, 2018, **29**(8), 6853–6869, DOI: 10.1007/s10854-018-8672-5.

28 Z. Zhu, C. Wei, D. Jiang, X. Wu and M. Lu, Design and synthesis of MOF-derived CuO/g-C3N4composites with octahedral structures as advanced anode materials for asymmetric supercapacitors with high energy and power densities, *Mater. Adv.*, 2022, **3**(1), 672–681, DOI: 10.1039/d1ma00766a.

29 J. R. Hu, J. W. Zhou, Y. X. Jia and S. Li, Cu-modified biomass-derived activated carbons for high performance supercapacitors, *New Carbon Mater.*, 2022, **37**(2), 412–423, DOI: 10.1016/S1872-5805(22)60602-4.

30 D. Li, *et al.*, Copper Oxide Nitrogen-Rich Porous Carbon Network Boosts High-Performance Supercapacitors, *Metals*, 2023, **13**(5), 981, DOI: 10.3390/met13050981.

31 S. Sirisomboonchai, S. Kongparakul, P. Reubroycharoen, G. Guan, H. Zhang and C. Samart, Fabrication of a Copper/Carbon Composite Based on Biomass for Electrochemical Application, *J. Japan Inst. Energy*, 2017, **96**(8), 273–278, DOI: 10.3775/jie.96.273.

32 Y. Zhan, *et al.*, Facile synthesis of biomass-derived porous carbons incorporated with CuO nanoparticles as promising electrode materials for high-performance supercapacitor applications, *J. Alloys Compd.*, 2021, **885**, 161014, DOI: 10.1016/j.jallcom.2021.161014.

33 S. Ravichandran, J. Radhakrishnan, P. Sengodan and R. Rajendran, Biosynthesis of copper oxide nanoparticle from clerodendrum phlomidis and their decoration with graphene oxide for photocatalytic and supercapacitor application, *J. Mater. Sci. Mater. Electron.*, 2022, **33**(12), 9403–9411, DOI: 10.1007/s10854-021-07340-0.

34 F. Wu, J. Gao, S. Zuo, W. Wang and H. Qiu, Cu2O-loaded heteroatom-doped worm-like hierarchical porous carbon flakes for high-performance energy storage devices, *Chem. Eng. Sci.*, 2021, **236**, 116530, DOI: 10.1016/j.ces.2021.116530.

35 D. Mohanadas, M. A. A. Mohd Abdah, N. H. N. Azman, J. Abdullah and Y. Sulaiman, A promising negative electrode of asymmetric supercapacitor fabricated by incorporating copper-based metal-organic framework and reduced graphene oxide, *Int. J. Hydrogen Energy*, 2021, **46**(71), 35385–35396, DOI: 10.1016/j.ijhydene.2021.08.081.

36 X. Zhang, *et al.*, High-power and high-energy-density flexible pseudocapacitor electrodes made from porous CuO nanobelts and single-walled carbon nanotubes, *ACS Nano*, 2011, **5**(3), 2013–2019, DOI: 10.1021/nn1030719.

37 M. Vandana, H. Vijeth, S. P. Ashokkumar and H. Devendrappa, Effect of Different Gel Electrolytes on Conjugated Polymer - Graphene Quantum Dots Based Electrode for Solid State Hybrid Supercapacitors, *Polym. Technol. Mater.*, 2020, 2068–2075, DOI: 10.1080/25740881.2020.1784221.

38 Y. S. Nagaraju, H. Ganesh, S. Veeresha, H. Vijeth and H. Devendrappa, Synthesis of hierarchical ZnO/NiO nanocomposite Wurtz hexagonal nanorods *via* hydrothermal for high-performance symmetric supercapacitor application, *J. Energy Storage*, 2022, **56**(PA), 105924, DOI: 10.1016/j.est.2022.105924.

39 A. B. shbil, *et al.*, Bio-waste-derived one-step carbonized hierarchical structured carbon/cobalt oxide composite for energy storage application, *Ionics*, 2025, **31**(3), 2563–2576, DOI: 10.1007/s11581-025-06072-z.

40 H. Vijeth, S. P. Ashokkumar, L. Yesappa, M. Niranjana, M. Vandana and H. Devendrappa, Camphor sulfonic acid assisted synthesis of polythiophene composite for high energy density all-solid-state symmetric supercapacitor, *J. Mater. Sci. Mater. Electron.*, 2019, **30**(8), 7471–7484, DOI: 10.1007/s10854-019-01060-2.

41 B. Approach, G. Ricardo, S. C. Sousa, Ó. L. Ramos, D. A. Campos and N. Aguilar, Obtention and Characterization of Microcrystalline Cellulose from Industrial Melon Residues Following a Biorefinery Approach, *Molecules*, 2024, **29**, 3285, DOI: 10.3390/molecules29143285.

42 M. Dev and M. Mukadam, Functional group profiling of medicinal plants using FTIR spectroscopy, *World J. Biol. Pharm. Heal. Sci.*, 2025, **21**(1), 243–249, DOI: 10.30574/wjbphs.2025.21.1.0039.

43 L. Hakim and E. Sedyadi, Synthesis and Characterization of Fe3O4 Composites Embeded on Coconut Shell Activated Carbon, *JKPK Jurnal Kim. dan Pendidik. Kim.*, 2020, **5**(3), 245, DOI: 10.20961/jkpk.v5i3.46543.

44 D. Renuga, J. Jeyasundari, A. S. Shakthi Athithan and Y. Brightson Arul Jacob, Synthesis and characterization of copper oxide nanoparticles using Brassica oleracea var. italic extract for its antifungal application, *Mater. Res. Express*, 2020, **7**(4), 045007, DOI: 10.1088/2053-1591/ab7b94.

45 Y. Cai, *et al.*, Facile Synthesis of Three-Dimensional Heteroatom-Doped and Hierarchical Egg-Box-Like Carbons Derived from Moringa oleifera Branches for High-Performance Supercapacitors, *ACS Appl. Mater. Interfaces*, 2016, **8**(48), 33060–33071, DOI: 10.1021/acsami.6b10893.

46 F. Su, L. Lv and X. S. Zhao, Synthesis of nanostructured porous carbon, *Int. J. Nanosci.*, 2005, **4**(2), 261–268, DOI: 10.1142/S0219581X05003127.

47 K. Chhetri, *et al.*, Integrated hybrid of graphitic carbon-encapsulated Cu x O on multilayered mesoporous carbon from copper MOFs and polyaniline for asymmetric

supercapacitor and oxygen reduction reactions, *Carbon*, 2021, **179**, 89–99, DOI: 10.1016/j.carbon.2021.04.028.
48 Y. Wang, S. Yang, Y. Yue and S. Bian, Conductive copper-based metal-organic framework nanowire arrays grown on graphene fibers for flexible all-solid-state supercapacitors, *J. Alloys Compd.*, 2020, **835**, 155238, DOI: 10.1016/j.jallcom.2020.155238.
49 S. Jha, *et al.*, Hydrogen-bond-guided micellar self-assembly-directed carbon superstructures for high-energy and ultralong-life zinc-ion hybrid capacitors, *J. Mater. Chem. A*, 2025, **13**(20), 15101–15110, DOI: 10.1039/d5ta00357a.
50 S. J. Rajasekaran and V. Raghavan, Facile synthesis of activated carbon derived from Eucalyptus globulus seed as efficient electrode material for supercapacitors, *Diam. Relat. Mater.*, 2020, **109**, 108038, DOI: 10.1016/j.diamond.2020.108038.
51 G. Zhuang, Y. Sun and X. Chen, CuS cluster microspheres anchored on reduced graphene oxide as electrode material for asymmetric supercapacitors with outstanding performance, *J. Mater. Sci. Mater. Electron.*, 2021, **32**(4), 4805–4814, DOI: 10.1007/s10854-020-05219-0.
52 A. M. Alturki, Benign feature for copper oxide nanoparticle synthesis using sugarcane molasses and its applications in electrical conductivity and supercapacitor, *Biomass Convers. Biorefin.*, 2022, 0123456789, DOI: 10.1007/s13399-022-03303-5.
53 L. Zhang, *et al.*, Facile synthesis of bio-based nitrogen- and oxygen-doped porous carbon derived from cotton for supercapacitors, *RSC Adv.*, 2018, **8**(7), 3869–3877, DOI: 10.1039/c7ra11475c.
54 A. S. Rajpurohit, N. S. Punde and A. K. Srivastava, A dual metal organic framework based on copper-iron clusters integrated sulphur doped graphene as a porous material for supercapacitor with remarkable performance characteristics, *J. Colloid Interface Sci.*, 2019, **553**, 328–340, DOI: 10.1016/j.jcis.2019.06.031.
55 T. G. Lim, T. Y. Kim and J. W. Suk, Activated graphene deposited on porous cu mesh for supercapacitors, *Nanomaterials*, 2021, **11**(4), 893, DOI: 10.3390/nano11040893.
56 S. G. Sayyed, A. V. Shaikh, U. P. Shinde, P. Hiremath and N. Naik, Copper oxide-based high-performance symmetric flexible supercapacitor: potentiodynamic deposition, *J. Mater. Sci. Mater. Electron.*, 2023, **34**(17), 1361, DOI: 10.1007/s10854-023-10738-7.
57 M. S. Lal, T. Lavanya and S. Ramaprabhu, An efficient electrode material for high performance solid-state hybrid supercapacitors based on a Cu/CuO/porous carbon nanofiber/TiO2 hybrid composite, *Beilstein J. Nanotechnol.*, 2019, **10**, 781–793, DOI: 10.3762/BJNANO.10.78.
58 W. Zhang, *et al.*, One-step facile solvothermal synthesis of copper ferrite-graphene composite as a high-performance supercapacitor material, *ACS Appl. Mater. Interfaces*, 2015, 7(4), 2404–2414, DOI: 10.1021/am507014w.
59 M. Zhou, J. Catanach, J. Gomez, S. Richins and S. Deng, Effects of Nanoporous Carbon Derived from Microalgae and Its CoO Composite on Capacitance, *ACS Appl. Mater. Interfaces*, 2017, **9**(5), 4362–4373, DOI: 10.1021/acsami.6b08328.
60 M. Zhai, A. Li and J. Hu, CuO nanorods grown vertically on graphene nanosheets as a battery-type material for high-performance supercapacitor electrodes, *RSC Adv.*, 2020, **10**(60), 36554–36561, DOI: 10.1039/d0ra06758j.
61 B. Saravanakumar, C. Radhakrishnan, M. Ramasamy, R. Kaliaperumal, A. J. Britten and M. Mkandawire, Copper oxide/mesoporous carbon nanocomposite synthesis, morphology and electrochemical properties for gel polymer-based asymmetric supercapacitors, *J. Electroanal. Chem.*, 2019, **852**, 113504, DOI: 10.1016/j.jelechem.2019.113504.
62 T. Lavanya and S. Ramaprabhu, Copper nanoparticles incorporated porous carbon nanofibers as a freestanding binder-free electrode for symmetric supercapacitor with enhanced electrochemical performance, *Mater. Res. Express*, 2019, **6**(10), 105005, DOI: 10.1088/2053-1591/ab3569.
63 V. H. Luan, J. H. Han, H. W. Kang and W. Lee, Highly porous and capacitive copper oxide nanowire/graphene hybrid carbon nanostructure for high-performance supercapacitor electrodes, *Composites, Part B*, 2019, **178**, 107464, DOI: 10.1016/j.compositesb.2019.107464.